

---

# <sup>1</sup> Chapter 1

## <sup>2</sup> The LHC and the ATLAS Detector

### <sup>3</sup> 1.1 The Large Hadron Collider

<sup>4</sup> The Large Hadron Collider (LHC) [1] is a proton ring collider located at the European Centre  
<sup>5</sup> for Nuclear Research (CERN). The main LHC ring is housed in the tunnel which previously  
<sup>6</sup> contained the Large Electron-Positron collider. The LHC ring is 27 km in circumference and  
<sup>7</sup> located approximately 175 m underground. The LHC services four different experiments lo-  
<sup>8</sup>cated at four interaction points around the beam-pipe (Figure 1.1). A toroidal LHC apparatus  
<sup>9</sup>(ATLAS, the experiment used for this thesis), the compact muon solenoid (CMS), a large ion  
<sup>10</sup> collider (ALICE) experiment and the LHC beauty (LHCb) experiment.

<sup>11</sup> ATLAS and CMS are general purpose detectors designed to support a varied physics pro-  
<sup>12</sup>gramme, from SM physics like top quark measurements to BSM searches such as supersym-  
<sup>13</sup>metry. ALICE and LHCb are more specialized experiments which focus on heavy ions and  $b$   
<sup>14</sup>physics, respectively.

<sup>15</sup> The LHC accelerates two beams of protons in opposite directions and then collides the two  
<sup>16</sup>beams at the four interaction points where the experiments are located. The protons come  
<sup>17</sup>from hydrogen gas where the orbiting electron is removed by an electric field, leaving behind  
<sup>18</sup>a bare proton. The beam acceleration occurs in several stages exploiting smaller experiments  
<sup>19</sup>present at CERN. During 2010 and 2011 protons were accelerated to a beam energy of 3.5 TeV,  
<sup>20</sup>creating a centre-of-mass energy of 7 TeV and then 4 TeV per beam in 2012 for a centre-of-  
<sup>21</sup>mass energy of 8 TeV. Each beam is made of multiple bunches of protons, with as many as  
<sup>22</sup>hundreds of billions of protons in each bunch. Bunches are grouped into *bunch trains* with a

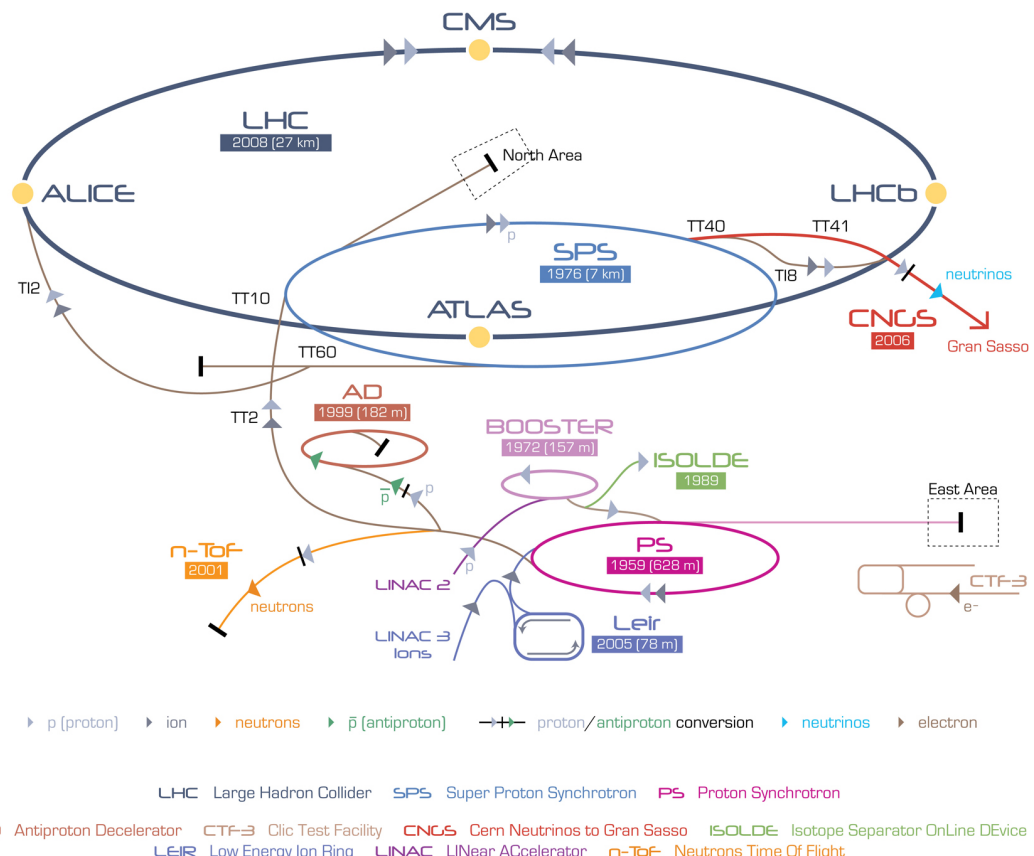
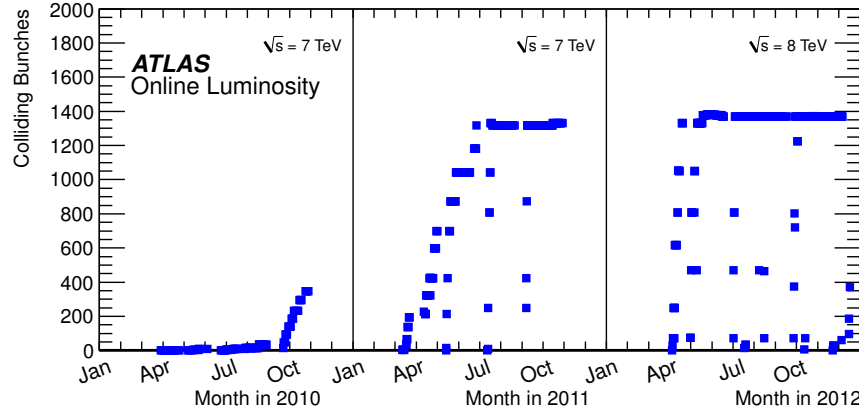
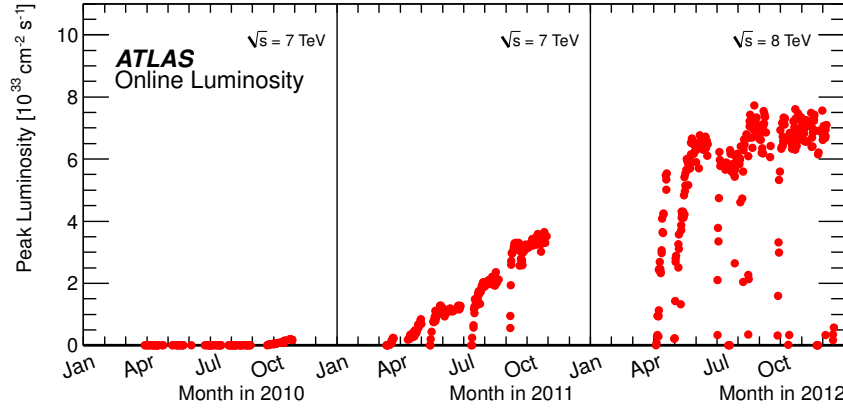


Figure 1.1: The layout of CERN complex of experiments, note the main four LHC experiments located at different points around the ring.

designed *bunch spacing* of 25 ns between each of the bunches that compose a single train. Note that the bunch spacing and size of the bunch can be altered to adjust the amount of collisions and the time between collisions. The variation in the number of colliding bunches is shown in Figure 1.2a.



(a) The number of bunches colliding per unit time at the LHC for the 2010, 2011 and 2012  $pp$  collision periods.



(b) The peak luminosity per unit time at the LHC for the 2010, 2011 and 2012  $pp$  collision periods.

Figure 1.2: Shown in (a) is the number of bunches colliding at the LHC and (b) the peak luminosity per unit time.

The acceleration of the proton beams occurs in several stages, within several different accelerators. The beams are first accelerated in a linear collider (LINAC 2) to an energy of 50 MeV before being injected into the proton synchotron booster (PSB). The beams are then boosted to 1.4 GeV by a varying magnetic field in the circular PSB. The beams are then passed into the proton synchrotron (PS) and then the super proton syncrotron (SPS) where the beam energy increases to 26 GeV and then 450 GeV. At this stage the beam is injected into the LHC and

then accelerated to the final desired energy. The design energy is 7 TeV per beam for a total of 14 GeV centre-of-mass energy. From injection of the protons into LINAC 2 to stable beam conditions in the LHC, the whole process can take a couple of hours.

As bunches overlap the protons that make up the bunches interact, these interactions are known as events. The number of events is proportional to the instantaneous luminosity  $\mathcal{L}$  of the collider.  $\mathcal{L}$  is a measure of the flux of particles per unit area per unit time can be defined as:

$$\mathcal{L} = f n_b \frac{N_1 N_2}{A} \quad (1.1)$$

where  $f$  is the frequency of revolution of the beam,  $n_b$  the number of colliding pairs of bunches in the beam,  $N_1$  and  $N_2$  are the number of particles in each colliding bunch and  $A$  is the cross-section of the beam [2]. The peak luminosity evolution at the LHC is shown in Figure 1.2b. Note that the operational  $\sqrt{s}$  of the LHC was 7 TeV for 2010/11 and 8 TeV for 2012.

The total amount of data collected is measured by the integrated luminosity  $\mathcal{L}_{\text{int}}$  defined as the time integral of  $\mathcal{L}$ . Integrated luminosity has units of inverse area, usually expressed in terms of barns (b)<sup>1</sup>. The probability for a given process to occur is expressed as the cross-section  $\sigma$  and the total number of events which proceed via said process is defined as:

$$\sigma \int \mathcal{L} dt \quad (1.2)$$

The integrated luminosity delivered by the LHC and collected by the ATLAS detector in 2011 and 2012 is shown in Figure 1.3. The ATLAS detector does not record all data delivered by the LHC; approximately 6.5% was not recorded.

### 1.1.1 Pileup

Due to the large number of interactions and the short time between collisions, multiple events can overlap into a single event. This has detrimental effects on physics analyses and is a determining factor in setting the instantaneous luminosity with which to perform data collection. This overlapping effect is collectively known as pileup and is categorized into two types: in-time pileup, where multiple  $pp$  collisions occur during the same bunch crossing; and out-of-time pileup, where the electric signals produced by a previous collision is still present in the

---

<sup>1</sup>  $1 b^{-1} = 10^{-28} m^{-2}$

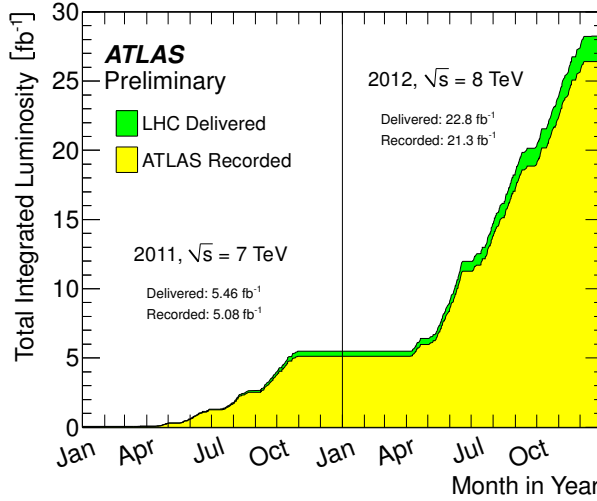


Figure 1.3: Distribution of the total integrated luminosity delivered by the LHC and the recorded by ATLAS for the 2011 and 2012  $pp$  collision period. Note the  $\sqrt{s}$  changing from 7 TeV to 8 TeV between 2011 and 2012.

57 detector. The number of interactions per crossing  $\mu$  is shown in Figure 1.4, note that on average  
 58 approximately thirty interactions occurred per bunch crossing in 2012. In comparison, in 2011  
 59 the average interactions per bunch crossing  $\langle \mu \rangle$  varied from  $\langle \mu \rangle = 5$  in early 2011 to  
 60  $\langle \mu \rangle = 15$  at the end of the year. The large number of overlapping events has a detrimental  
 61 effect on physics analyses and thus is an important factor when setting the operational  $\mathcal{L}$  of  
 62 the collider.

## 63 1.2 The ATLAS detector

64 The ATLAS [3] experiment is a general-purpose detector which wraps around the IP providing  
 65 large angular coverage. ATLAS is approximately cylindrical with a diameter of 25 m, a total  
 66 length of 44 m and weighs 7000 t. The detector is made of several layers of instrumentation  
 67 located at successively increasing radii as shown in Figure 1.5:

- 68 1. **Inner Detector:** Located nearest to the beam-pipe and designed to measure the track of  
 69 charged-particles.
- 70 2. **EM Calorimeter:** Used for identification and measurement of electrons and photons.
- 71 3. **Hadronic Calorimeter:** Used for the measurement of hadronic activity from hadroniz-

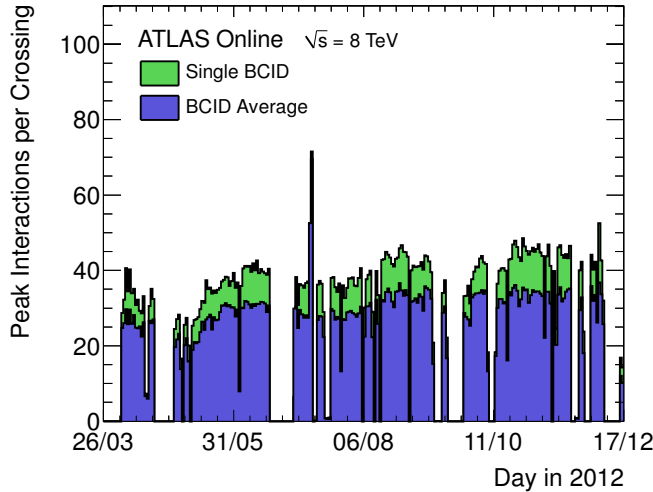


Figure 1.4: Number of interactions per bunch for the 2012  $pp$  data-taking period at ATLAS per day. Note that both the average number of interactions for all bunches and the maximum number of interactions are shown.

72 ing partons and missing transverse energy.

73 **4. Muon Spectrometer:** The outermost detection layer, used for muon identification and  
74 measurement.

75 Between these detection layers are magnets responsible for bending the path of the charged  
76 particles for the purpose of momentum measurement and particle identification. Additionally  
77 triggering and data acquisition (DAQ) systems form part of the detector for the purposes of  
78 recording the data signals coming from the aforementioned tracking and measurement sys-  
79 tems. A brief description of these systems is provided in the coming sections. For a more  
80 detailed technical description of the detector and all subsystems see [4].

81 Semi-leptonic  $t\bar{t}$  events produce a final state that includes hadronic activity, electrons,  
82 muons and missing energy and thus all elements of the detector are used in the reconstruction  
83 of such events. Additionally the match  $\chi^2_{\text{match}}$ -tagger which is central to this thesis relies on the  
84 reconstruction and fitting of inner detector tracks and muon spectrometer tracks. A detailed  
85 description of this algorithm is provided in the Chapter ??.

86 A cylindrical coordinate system as used by all ATLAS publications has been adopted here.  
87 The coordinate system is constructed so that the  $z$ -axis is parallel to the beam axis. The  $x$ -axis  
88 is positive in the direction going from the IP to the centre of the LHC ring, and the positive

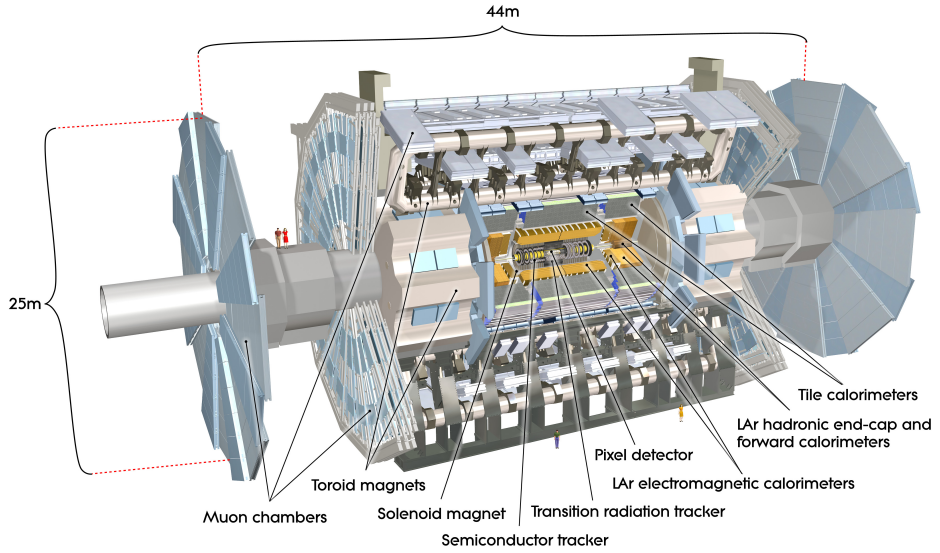


Figure 1.5: An overview diagram of the ATLAS experiment. Shown are all detection and tracking systems and the toroid magnet which encompasses them. Note also the muon system on the outside of the detector.

89  $y$ -axis points upwards. Thus the  $x - y$  plane is transverse to the beam direction. All transverse  
 90 variables such as the transverse momentum  $p_T$ , transverse energy  $E_T$  and missing transverse  
 91 energy  $\cancel{E}_T$  are measured along this plane. The azimuthal angle  $\phi$  is measured around the beam  
 92 axis, and the polar angle  $\theta$  is the angle from the beam axis. The pseudorapidity is defined as  
 93  $\eta = -\ln \tan(\theta/2)$ . The distance in the  $\phi$ - $\eta$  plane between two objects is denoted by  $\Delta R$  and  
 94 defined as  $\Delta R = \sqrt{\Delta\phi^2 + \Delta\eta^2}$ . Finally side A of the detector is defined as the positive  $z$  side  
 95 and side C is the negative  $z$ .

### 96 1.2.1 Inner Detector

97 The inner detector (ID) is a tracking detector located closest to the beam-pipe and used for  
 98 momentum and impact parameter measurement, vertex and track reconstruction and particle  
 99 identification. The ID is designed to provide hermetic, high-resolution tracking in the range  
 100  $|\eta| < 2.5$ . All components of the ID subsystem are shown in Figure

101 The entire ID is contained within the central solenoid (CS) that generates a 2 T magnetic  
 102 field for the purpose of momentum measurement. The trajectory of a charged particle is bent  
 103 in the presence of a magnetic field. The str by a magnitude dependent on the momentum of  
 104 the particle. By reconstructing this trajectory the momentum can be measured.

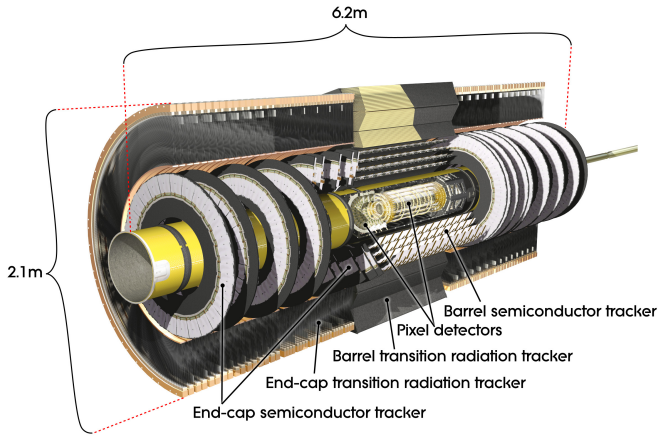


Figure 1.6: caption

105     The reconstruction of interaction vertices is of paramount importance, particularly when  
 106    considering the large amount of pile-up observed at ATLAS. Interaction vertices are recon-  
 107    structed by fitting all reconstructed tracks to a point. The primary vertex (PV) is then defined  
 108    as the vertex with the largest amount of momentum associated with it. In addition the recon-  
 109    struction of secondary interaction vertices is used for the identification of short-lived particles  
 110    such as  $B$ -hadrons and  $\tau$ .

111     The ID is made of three separate tracking and detection systems located at increasing radii  
 112    away from the beam-pipe, the full arrangement can be seen in Figure 1.8 and a plane-view is  
 113    shown in Figure 1.9.

#### 114   **Pixel detector**

115     The pixel detector is located nearest to the beam-pipe and provides high-granularity and pre-  
 116    cision for secondary vertex reconstruction. It consists of three silicon pixel sensors layers in  
 117    the barrel region located at approximately 5 cm, 9 cm and 12 cm from the IP, and three disks  
 118    at each side located at constant  $R$  providing coverage up to  $|\eta| < 2.5$ . The barrel modules are  
 119    overlapped in a turbine pattern to provide hermetic coverage. In the barrel region the modules  
 120    provide an intrinsic resolution of  $10 \mu\text{m}$  in  $R - \phi$  and  $115 \mu\text{m}$  in  $z$ . The disk sections have an  
 121    intrinsic resolution of  $10 \mu\text{m}$  ( $R - \phi$ ) and  $115 \mu\text{m}$  ( $R$ ).

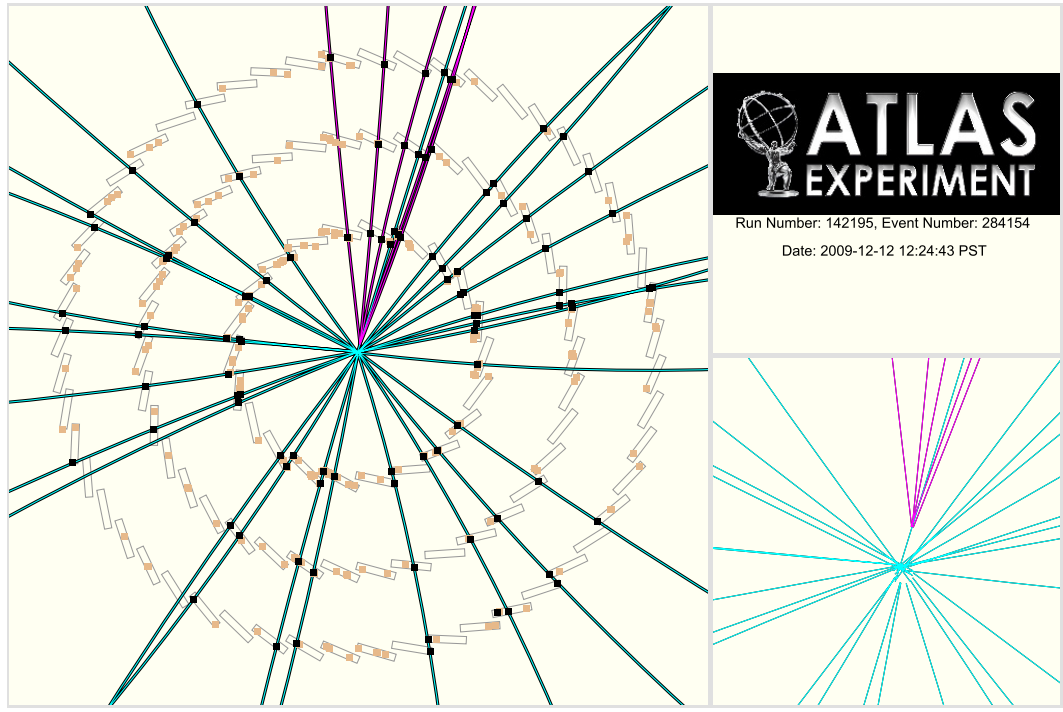


Figure 1.7: An event-display of an event as reconstructed by the ATLAS inner detector. Shown are the results of the vertexing algorithm where each line represents a track. the purple tracks have been fitted to a secondary vertex.

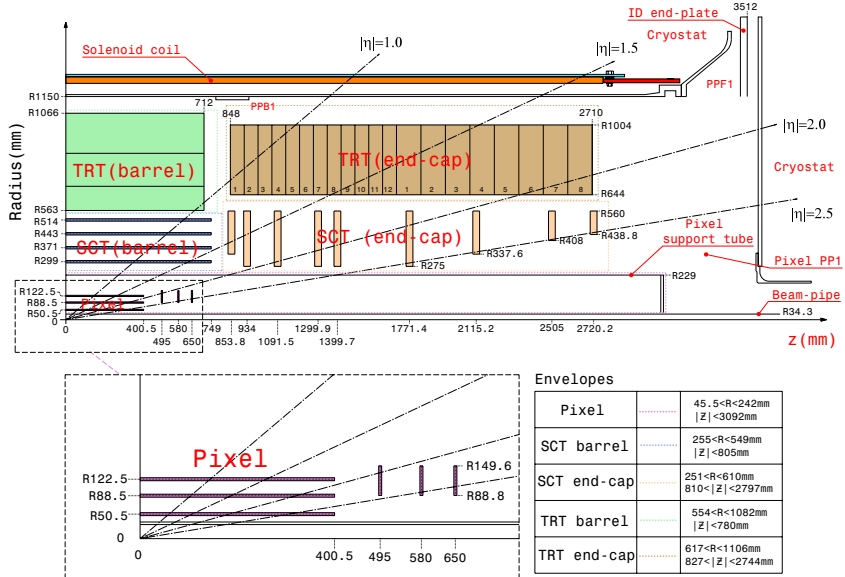


Figure 1.8: Plan-view of a quarter-section of the ATLAS ID showing the major detector elements with its active dimensions and envelopes. Note also the  $\eta$  markers showing the maximum coverage up to  $\eta = 2.5$ .

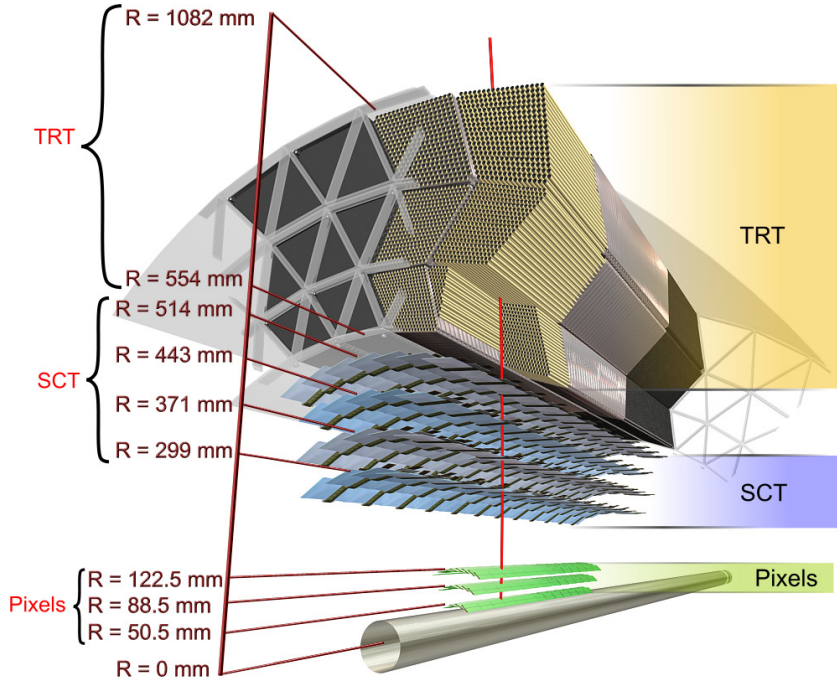


Figure 1.9: A drawing of in the transverse plane of the ATLAS ID showing all major detection elements in the barrel regions. Note the charged particle track marked in red traversing all the detector elements.

### 122 Semiconductor tracker

123 The semiconductor tracker (SCT) located in the intermediate radius range is designed to pro-  
124 vide eight hits per track contributing to the measurement of momentum, impact parameter  
125 and vertex position. The SCT is made of four layers of stereo-pair silicon micro-strip sensors  
126 in the barrel region at increasing radii with an intrinsic resolution of  $17\text{ }\mu\text{m}$  ( $R - \phi$ ) and  $580\text{ }\mu\text{m}$   
127 ( $z$ ). At the end-caps nine disks of silicon microstrip modules provide large  $\eta$  coverage with a  
128 resolution of  $17\text{ }\mu\text{m}$  ( $R - \phi$ ) and  $580\text{ }\mu\text{m}$  ( $R$ ).

### 129 Transition radiation tracker

130 The transition radiation tracker (TRT) is the outermost tracking layer that forms the inner  
131 detector. The TRT is designed to provide up to 36 hits per track using straw-tube sensors. In  
132 the barrel the 144 cm long straw-tubes are arranged in modules which contain between 329  
133 and 793 straws. The end-cap disks are made of radially distributed 36 cm long straw-tubes.  
134 Each straw-tube provides an intrinsic resolution of  $130\text{ }\mu\text{m}$  along its length. The combination  
135 of a large number of hits over a large radius allows for measurements in the TRT to be made

<sup>136</sup> with an accuracy that can complement those made by the pixel detector.

<sup>137</sup> **1.2.2 Calorimetry**

<sup>138</sup> The ATLAS calorimeter is responsible for the measurement of the energy of particles that  
<sup>139</sup> emerge from the event. Sampling calorimeters are used for this purpose, layers of absorber  
<sup>140</sup> material (passive) are placed in the path of the particles forcing them to interact and shower.  
<sup>141</sup> The amount of energy lost by the incident particle depends on the type of material the particle  
<sup>142</sup> traverses, the energy of the particle and the type. At high energies electrons lose energy pre-  
<sup>143</sup> dominantly via Bremsstrahlung, while photons lose energy via pair production. The character-  
<sup>144</sup> istic length associated with this energy loss is a material characteristic known as the radiation  
<sup>145</sup> length  $X_0$ .

<sup>146</sup> For electrons the energy as a function of material traversed is

$$E = E_0 e^{-x/X_0} \quad (1.3)$$

<sup>147</sup> where  $E$  is the energy of the incident particle,  $E_0$  is the original energy and  $x$  is the distance  
<sup>148</sup> traversed. As an electron traverses one  $X_0$  of material, its energy is reduced by a factor of  $1/e$ .  
<sup>149</sup> For photons the average number of photons traversing through a material length  $x$  is reduced  
<sup>150</sup> exponentially by a factor of  $\frac{7}{9}X_0$ .

<sup>151</sup> The energy of the resulting shower is then measured by some sampling material (active)  
<sup>152</sup> located behind the absorbers, this energy is proportional to the energy of the incident particle.

<sup>153</sup> The type and thickness of material used is varied through the pseudorapidity range to  
<sup>154</sup> improve energy measurement and reduce punch-through of particles into the muon systems  
<sup>155</sup> behind. Due to the large amount of intense radiation produced during collisions, radiation  
<sup>156</sup> hardness is also a driving factor in material choice.

<sup>157</sup> The ATLAS calorimeter consists of the electromagnetic (EM) calorimeter, designed to mea-  
<sup>158</sup> sure photons and electrons covering the pseudorapidity region  $|\eta| < 3.2$ ; the hadronic calorime-  
<sup>159</sup> ter (HCal), designed to measure hadronic activity covering the pseudorapidity region  $|\eta| < 3.2$ ;  
<sup>160</sup> and the forward calorimeter (FCal) which provides energy measurement capability in the very  
<sup>161</sup> high pseudorapidity region  $3.1 < |\eta| < 4.9$ . As can be seen in Figure 1.10 the calorimetry  
<sup>162</sup> envelopes the ID and CS providing hermetic coverage symmetric in  $\phi$ . This is particularly im-

<sup>163</sup> portant for the measurement of  $E_T$  resulting from weakly interacting particles escaping the  
<sup>164</sup> detector.

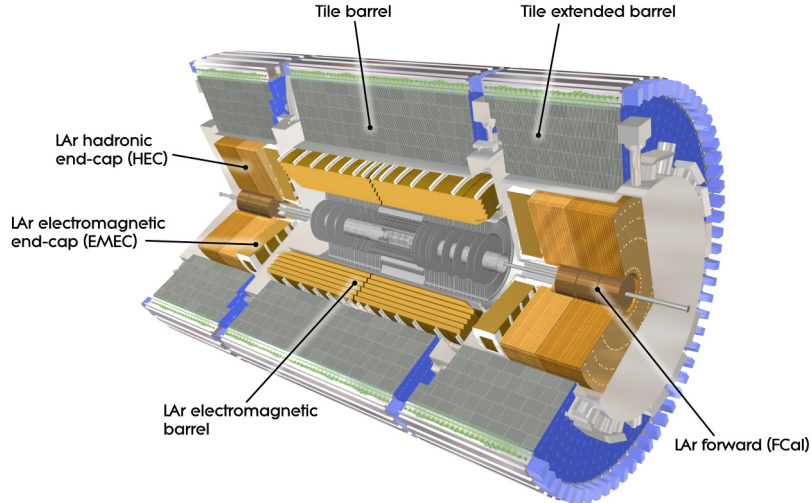


Figure 1.10: A cut-away diagram of the ATLAS detector highlighting the calorimetry system. Shown are the ECal barrel and end-cap, the HCal barrel and end-cap and the FCal end-cap.

### <sup>165</sup> Electromagnetic calorimeter

<sup>166</sup> The EM calorimeter is made of a barrel section ( $|\eta| < 1.475$ ) and two end-caps ( $1.375 <$   
<sup>167</sup>  $|\eta| < 3.2$ ). The EM barrel consists of two half-barrels separated by a 4 mm gap at  $z = 0$ .  
<sup>168</sup> The end-caps consist of two coaxial wheels, the outer ring covering the pseudorapidity range  
<sup>169</sup>  $1.375 < |\eta| < 2.5$  and the inner ring covering the range  $2.5 < |\eta| < 3.2$ . The pseudorapidity  
<sup>170</sup> region  $1.37 < |\eta| < 1.52$  is not used for precision physics due to the large amount of material,  
<sup>171</sup> this is known as the “crack” region.

<sup>172</sup> The EM calorimeter employs liquid Argon (LAr) as the active material due to its intrinsic  
<sup>173</sup> radiation hardness and response over time, and lead as the passive material arranged in an  
<sup>174</sup> accordion geometry for full  $\phi$  symmetry. Particles interact with the lead absorbers creating a  
<sup>175</sup> shower which ionizes the layers of liquid Argon. A potential is applied across the LAr mate-  
<sup>176</sup> rial allowing for signal readout via Kapton/copper electrodes. The total thickness of the EM  
<sup>177</sup> calorimeter is  $> 24X_0$  in the barrel and  $> 26X_0$  in the end-caps. The amount of material is  
<sup>178</sup> optimized in pseudorapidity to enhance energy resolution.

<sup>179</sup> In the region devoted to precision physics the EM calorimeter is divided into three seg-

Table 1.1: Design energy resolution of all ATLAS calorimeter components. The resolution is made of a sampling term ( $1/\sqrt{E}$ ) associated with the choice of passive and active materials and construction of the layers and a constant term associated with the depth of the detector, cracks and dead material.

Section	Resolution
EM Barrel	$\frac{10\%}{\sqrt{E}} \oplus 0.7\%$
EMEC	$\frac{10\%}{\sqrt{E}} \oplus 0.7\%$
HEC	$\frac{100\%}{\sqrt{E}} \oplus 10\%$
FCAL	$\frac{100\%}{\sqrt{E}} \oplus 10\%$

ments as shown in Figure 1.11, the strip layer is designed to improve particle identification and pseudorapidity position measurement. The design energy resolution for all components of the calorimeter are shown in Table 1.1.

### Hadronic calorimeter

The hadronic calorimeter uses different types of passive and active material to accomodate for the varying conditions in different regions of the detector. The materials used and structure of the detector must provide good energy resolution, full symmetric coverage for the purpose of  $E_T$  measurement, full containment of all hardonic activity to prevent punch-through to the muon system and be sufficiently radiation hard.

The hadronic calorimeter consists of two parts a scintillator tile calorimeter in the barrel region, and a LAr calorimeter in the end-cap.

The tile calorimeter is located directly outside the EM calorimeter. The barrel portion of the calorimeter covers the region  $|\eta| < 1.0$  and the two extended barrels cover the range  $0.8 < |\eta| < 1.7$ . The tile calorimeter uses steel as the passive material and scintillating tiles as the active material. The resulting hadronic showers enter the scintillating tiles and produce photons which are passed to photomultiplier tubes (PMTs). The total detector thickness which is tile-instrumented is 9.7 interaction lengths ( $\lambda$ ) at  $\eta = 0$ .

The hadronic end-cap (HEC) uses LAr technology due to its radiation-hardness in this challenging high pseudorapidity region. The HEC consists of two independent wheels per end-cap covering the range  $1.5 < |\eta| < 3.2$  overlapping the tile calorimeter at low pseudorapidity range and the forward calorimeter located at high pseudorapidity.

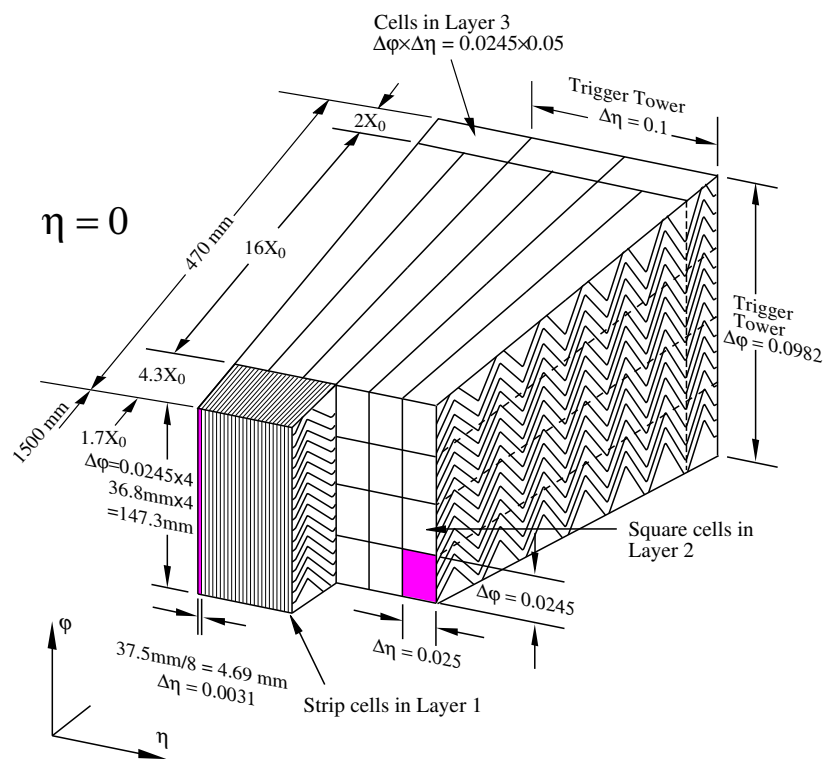


Figure 1.11: Cut-away diagram of the EM calorimeter barrel at  $\eta = 0$ . Shown are the three different layers with varying cell structures. The strip section is designed to enhance particle identification and position measurement in  $\eta$ .

**201    Forward calorimeter**

202    The forward calorimeter (FCal) is responsible for energy measurement in the very-high pseu-  
 203    dorapidity range  $3.1 < |\eta| < 4.9$  of both electromagnetic and hadronic activity. Due to the  
 204    large amount of radiation in this  $\eta$  region, LAr is employed as the active material. The FCal con-  
 205    sists of three layers, the first made primarily of copper, designed mostly for the measurement  
 206    of electromagnetic activity while the two outer tungsten layers are responsible for hadronic  
 207    activity measurement.

**208    1.2.3 Muon spectrometer**

209    The muon spectrometer (MS) is the outer most layer of the ATLAS detector (Figure 1.12) and  
 210    is responsible for the precision measurement of  $p_T$  of charged-particles that pass-through the  
 211    ATLAS calorimetry. Muon tracking performance is vital to the SMT tagger described in Sec-  
 212    tion ??, as it relies on the precise reconstruction of muon tracks in the ID and MS. Inner detector  
 213    tracks and Muon spectrometer tracks are fitted to form a *combined* muon track, the quality of  
 214    the fit is at the core of the SMT algorithm.

215    Due to their larger mass, muons tend to have a larger tranverse momentum and as such  
 216    do not lose as much energy through the emission of photons in the calorimetry. As a result,  
 217    muons tend to traverse the hadronic calorimeter and escape the detector volume. The muon  
 218    system provides measurement of these particles up to  $|\eta| < 2.7$  and triggering up to  $|\eta| < 2.4$ .  
 219    Measurement of  $p_T$  is facilitated by the magnetic field generated by the large toroid magnet  
 220    in the barrel region  $|\eta| < 1.4$  and two smaller end-cap magnets in  $1.6 < |\eta| < 2.7$ . In the  
 221    transition region ( $1.4 < |\eta| < 1.6$ ) deflection is provided by the barrel and end-cap fields.

222    The structure of the MS is delimited by the magnet system. In the barrel region three  
 223    cylindrical layers of precision-tracking chambers are located in and on the coils of the barrel  
 224    toroid magnet at radii of 5 m, 7.5 m and 10 m. End-cap region coverage is provided by three  
 225    chamber planes perpendicular to the  $z$ -axis located in front and behind the end-cap toroid  
 226    magnet at distances  $|z| \approx 7.4$  m, 10.8 m, 14 m and 21.5 m from the interaction point.

227    The MS contains four different types of chambers responsible for precision-tracking and/or  
 228    triggering in various pseudorapidity ranges as shown in Table 1.2. The arrangement of these  
 229    chambers is shown in Figure 1.13.

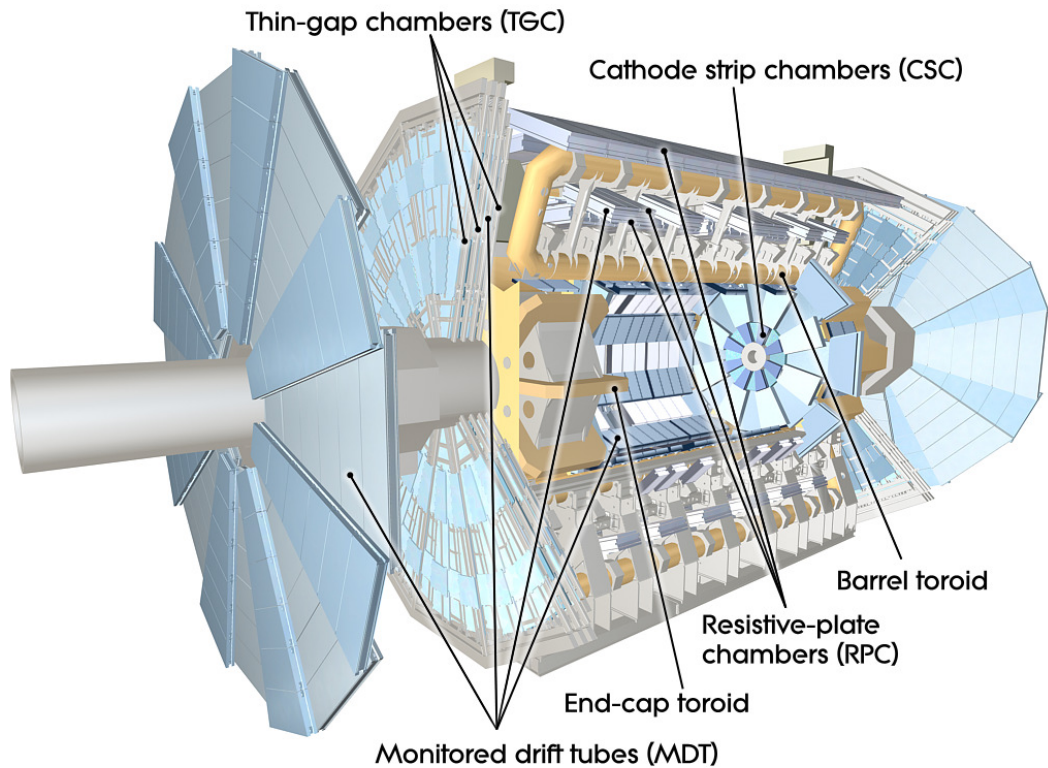


Figure 1.12: Cut-away drawing of the ATLAS muon system.

<b>Monitored drift tubes</b>	<b>MDT</b>
<ul style="list-style-type: none"> <li>- Coverage</li> <li>- Number of chambers</li> <li>- Function</li> </ul>	$ \eta  < 2.7$ (innermost layer: $ \eta  < 2.0$ ) 1150 Precision tracking
<b>Cathode strip chambers</b>	<b>CSC</b>
<ul style="list-style-type: none"> <li>- Coverage</li> <li>- Number of chambers</li> <li>- Function</li> </ul>	$2.0 <  \eta  < 2.7$ 32 Precision tracking
<b>Resistive place chambers</b>	<b>RPC</b>
<ul style="list-style-type: none"> <li>- Coverage</li> <li>- Number of chambers</li> <li>- Function</li> </ul>	$ \eta  < 1.05$ 606 Triggering, second coordinate
<b>Thin gap chambers</b>	<b>TGC</b>
<ul style="list-style-type: none"> <li>- Coverage</li> <li>- Number of chambers</li> <li>- Function</li> </ul>	$1.05 <  \eta  < 2.7$ (2.4 for triggering) 3588 Triggering, second coordinate

Table 1.2: Main parameters of the muon system.

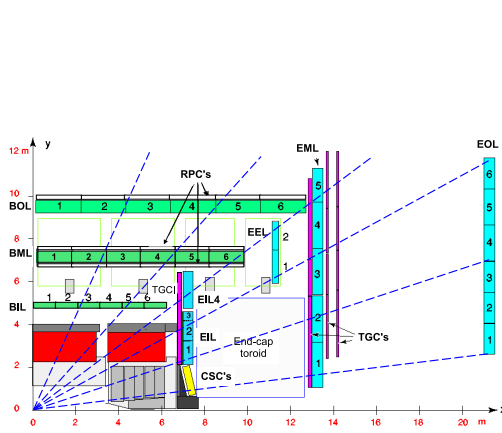


Figure 1.13: Plan view of quarter-section of the ATLAS muon spectrometer.

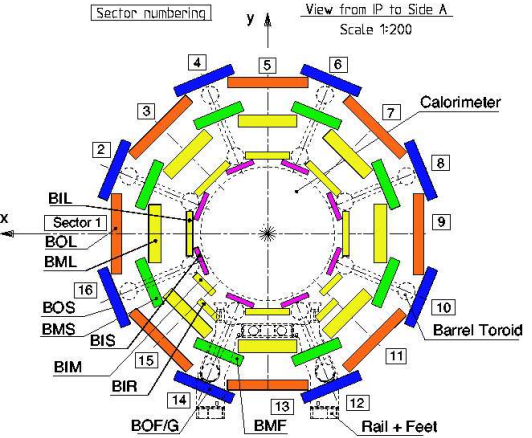


Figure 1.14: Transverse view of the muon system. Shown are the

230 In the barrel region, precision-measurement is performed by monitored drift tubes (MDT)  
 231 chambers. These chamber consist of three to eight pressurised aluminium drift tubes, each  
 232 containing a tungsten-rhenium wire anode and a mixture of argon and carbon dioxide gas. An  
 233 average spatial resolution of  $80 \mu\text{m}$  per tube and  $35 \mu\text{m}$  per chamber is achieved.

234 The end-cap region is instrumented with cathode-strip chambers (CSC) due to their higher  
 235 rate capability and time resolution. CSCs are multiwire chambers with cathode planes seg-  
 236 mented into strips in orthogonal directions. This allows for both coordinates to be measured  
 237 simultaneously. The resolution of a chamber is  $40 \mu\text{m}$  in the bending plane ( $R - z$ ) and  $5 \text{ mm}$   
 238 in the transverse plane.

239 Triggering on muon tracks is another essential role of the muon spectrometer. To this end,  
 240 each precision-measurement chamber is complemented with fast triggering chambers. As with  
 241 the measurement layers, two different types of chambers are used for the barrel and end-cap  
 242 regions. In the barrel region ( $|\eta| < 1.05$ ) resistive plate chambers (RPC) are used attached to the  
 243 same support structure as the MDTs. The RPCs are made of two resistive plates,  $2 \text{ mm}$  apart,  
 244 between which a potential difference is applied. The gap between the plates is filled with a  
 245 mixture of  $\text{C}_2\text{H}_2\text{F}_4/\text{Iso-C}_4\text{H}_{10}/\text{SF}_6$ . The signal is read out via metallic strips mounted to the  
 246 outer faces of the resistive plates. The end-cap region ( $1.05 < |\eta| < 2.4$ ) is populated with  
 247 thin gap chambers (TGC). TGCs multiwire chambers like those used in the CSC, however the  
 248 distance between the wire and the cathode is smaller in the TGC. A summary of the spatial  
 249 and temporal resolution for the measurement and triggering layers is shown in Table 1.3.

Type	$R/z$	$\phi$	time
MDT	35 $\mu\text{m}$ ( $z$ )	–	–
CSC	40 $\mu\text{m}$ ( $R$ )	5 mm	7 ns
RPC	10 mm ( $z$ )	10 mm	1.5 ns
TGC	2-6 mm ( $R$ )	3-7 mm	4 ns

Table 1.3: Summary of spatial and temporal resolutions per chamber for all chamber types used in the the ATLAS muon spectrometer. Adapted from [3].

#### 250 1.2.4 Magnet system

251 The structure of the ATLAS detector is defined by the large magnet system. The ATLAS magnet  
 252 system, shown in Figure 1.15, consists two sets of magnets. The central solenoid and three air-  
 253 core toroids.

254 The central solenoid located nearest to the beam, provides a 2 T magnetic field for the ID  
 255 for the purpose of tracking, particle identification and  $p_{\text{T}}$  measurement.

256 The barrel toroids extend to  $|\eta| < 1.4$  and are made of eight coils, generating a 0.5 T  
 257 magnetic field for the MS. In the high pseudorapidity range, magnetic deflection is provided  
 258 by two end-cap toroids extending from  $1.6 < |\eta| < 2.4$ . As in barrel, the end-cap toroids are  
 259 made of eight coils offset by  $22.5^\circ$  with respect to the barrel coils. Each end-cap generates a 1 T  
 260 magnetic field for the MS. The so-called transition region between the two magnets is covered  
 261 by an overlap of the end-cap and barrel fields.

#### 262 1.2.5 Triggering and DAQ

263 At the design luminosity of the LHC  $\mathcal{L}=10 \times 10^{34} \text{ cm}^{-2} \text{ s}^{-1}$ , the expected event rate is ap-  
 264 proximately 1 GHz. At an average event size of 1.3 MB per event, the total amount of data  
 265 produced at ATLAS is  $1.2 \text{ PB s}^{-1}$ . The maximum rate of data storage at ATLAS is approxi-  
 266 mately  $300 \text{ MB s}^{-1}$ , so the rate must be reduced.

267 The trigger and data acquisition system (TDAQ) is responsible for selecting only “inter-  
 268 esting” events for recording, thus reducing the rate. This is known as an *online selection* as it  
 269 happens before the data is stored. Selections during analysis for example, are known as *offline*  
 270 *selection*, as they happen after the data has been recorded.

271 The overwhelming majority of events produced at the LHC are of no interest to physics  
 272 analysis, for example the so-called *minimum bias events*.

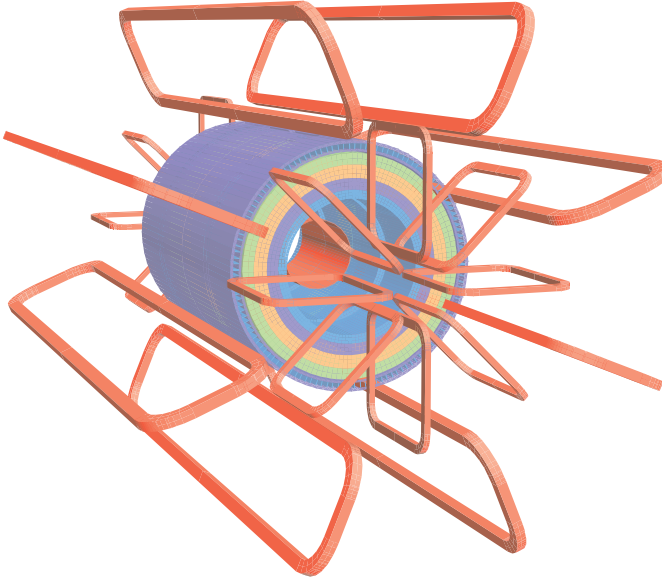


Figure 1.15: Diagram of the ATLAS toroid magnet system. The red central solenoid is located closest to the beam surrounded by layers of tile calorimetry. The eight barrel toroid magnets are shown along with the offset end-cap toroids at each end.

At ATLAS, trigger decisions are carried out in three sequential levels: *Level 1* (L1), *Level 2* (L2) and *Event Filter* (EF), each successive level reduces the rate by applying increasingly more complex selection criteria. The hardware-based L1 trigger, performs the initial selection based on reduced-granularity information from the MS trigger chambers and all calorimeters. Data from the calorimeter trigger towers, shown in Figure 1.11, is used to search for presence of high transverse-momentum muons, photons, electrons, hadronic decays of  $\tau$  leptons and hadronic jets, as well as large missing transverse energy and large total transverse energy. The central trigger processor applies the the trigger ‘menu’ which includes a combination of selection criteria. Events which are of interest to physics analyses can be produced at such a rate as to overwhelm the capabilities of the DAQ. A *prescale* can be applied to record one out of many of these events, thus reducing the rate. The L1 trigger also constructs *regions of interest* (RoIs) around the detector where interesting features have been found. The  $\eta$  and  $\phi$  information of the RoI along with information about the decision is stored and passed to the higher level triggers.

The L2 selection makes use of RoIs and the full granularity of the detector to further reduce the event rate to approximately 3.5 kHz and finally the EF implements selections commonly used for offline analysis to reduce the rate to 200 Hz.

## 290 1.3 Monte Carlo Simulation

291 The simulation of data is paramount to HEP research, from the initial detector design phase all  
 292 the way through to finalized analyses. Monte Carlo (MC) generators simulate various inter-  
 293 actions, creating kinematic collision event data that reflect our best understanding of nature.  
 294 These processes are then passed through detector simulation and all the object reconstruction  
 295 algorithms, resulting in a dataset with an identical format to collision data.

296 Simulation of data happens in three phases: event generation, detector simulation and  
 297 digitization.

### 298 1.3.1 Event Generation

299 Event generators are tools that model complex physics processes that occur during a particle  
 300 collision. Many different generators exist to model a variety of beam types ( $pp$ ,  $p\bar{p}$ ,  $e^+e^-$ ,  
 301 etc...) and event types. Hadronic event generation simulates all components which make up  
 302 the interaction, namely the hard scattering process, parton showering, hadronising, hadronic  
 303 decay, the underlying event and photon radiation [5] as shown in Figure 1.16.

304 First, the *hard interaction* of a pair of partons originating from the colliding protons is  
 305 simulated. An example of such an interaction is  $q\bar{q} \rightarrow Z/\gamma^* \rightarrow e^+e^-$ . Calculating the cross  
 306 section for such an interaction involves the convolution of the parton density function (PDF)  
 307 and the *matrix element* (ME).

308 The PDF  $f_i(x, Q^2)$ , describes the probability of finding, within the proton, a parton of  
 309 flavour  $i$  carrying a fraction  $x$  of the proton momentum, via a hard interaction with energy  
 310 scale  $Q$ . The ME describes the interaction between the two partons and corresponds to one  
 311 or more of the feynman diagrams associated with the interaction<sup>2</sup>. The order of a diagram is  
 312 determined by the number of coupling constants associated with it. Different generators are  
 313 capable of treating diagrams at different orders. The hard interaction is usually modelled at LO  
 314 or NLO.

315 The next step is *parton-showering* which simulates the emission of gluons by coloured par-  
 316 tons. A cascade of partons is produced, as shown in Figure 1.16, and modelled by perturbation  
 317 theory for energies above 1 GeV. All colored objects are then combined into colorless hadrons

---

<sup>2</sup>For a rigorous discussion of matrix elements and the Feynman rules, see [7,8]

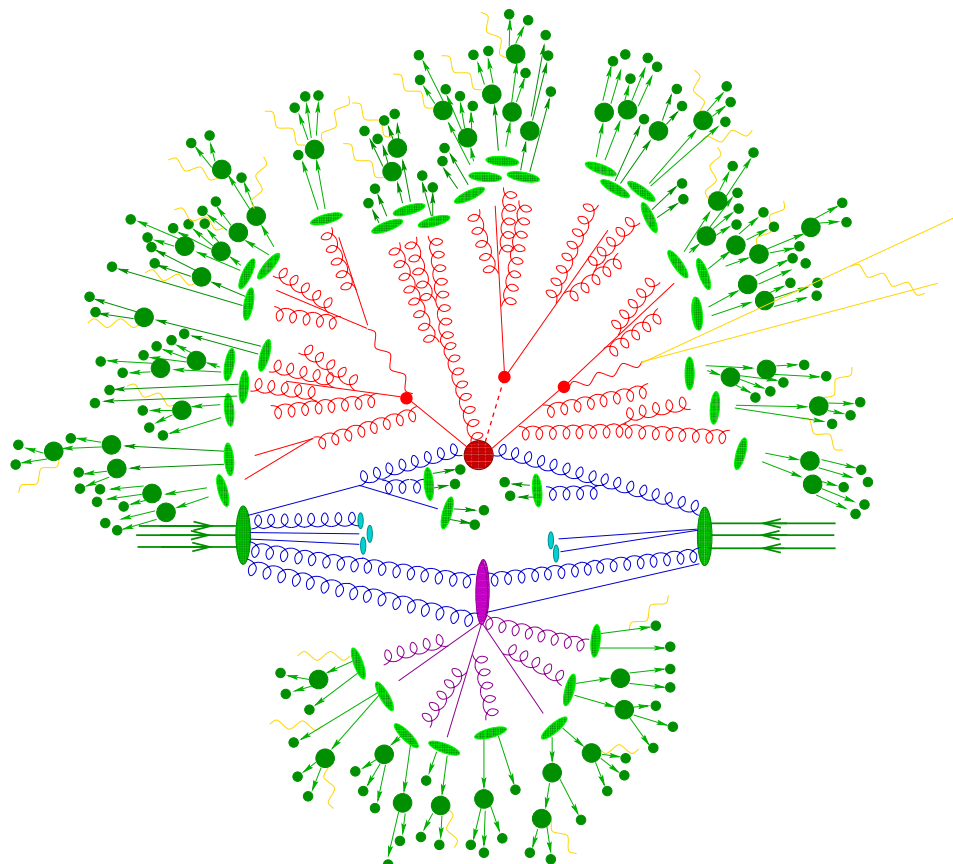


Figure 1.16: Sketch of a proton-proton collision as modelled by the event generator [6]. Shown are the incoming protons beams as green arrows on the left and right sides of the diagram. The partons shown in blue, interact in the hard interaction (red blob) producing a parton shower, also depicted in red, which eventually hadronize (light green blobs) and finally decay into final state particles shown in dark green. The *underlying event* is shown at the bottom of the diagram as the purple blob, note also the beam remnants as light blue blobs that also form part of the underlying event. Photon emission is shown in yellow and occurs at all stages of the event generation.

318 in a process known as *hadronization*, these hadrons are subsequently allowed to decay.

319 Finally, the remaining colored partons not involved in the hard interaction, are allowed to  
320 interact forming the *underlying event*.

321 The kinematic information of the original event without the effects of the detector is kept  
322 in the data set and is usually referred to as the *truth information*.

### 323 1.3.2 Detector simulation

324 The generated events are then passed through a detector simulation that mimicks the re-  
325 sponse of the detector to particles traversing through it. A description of the entire detector  
326 is implemented in the GEANT4 toolkit, including a map of the magnetic fields, the position  
327 of the detector components and material description. The software then simulates the signal  
328 voltages produced in all tracking and calorimeter components of the detector, these are then  
329 passed through a simulation of the read-out electronics and DAQ taking into account known  
330 losses and inefficiencies. All of this information is then passed on to the reconstruction software  
331 that “rebuilds” the physics objects from the detector *hits*.

## 332 1.4 Event reconstruction

333 The process of converting the raw data from the detector into formed events with physics  
334 objects (electrons, muons and so on) is known as *event reconstruction*. The algorithms for object  
335 reconstruction are identical for both collision data and simulated data. The focus of this thesis,  
336 the soft muon tagger, is used on *STACO combined* muons. Therefore some details of the muon  
337 reconstruction algorithms are discussed in the next section.

### 338 1.4.1 Muon reconstruction

339 Muon reconstruction can make use of the information provided by both the inner detector and  
340 the muon spectrometer systems. Several muon reconstruction strategies exist [9]:

- 341 • **Standalone reconstruction:** Uses MS information only, first constructing *segments*  
342 from several hits in a given chamber and then fitting segments from all three stations to  
343 hits from the four MS components. Tracks are then extrapolated back to the IP taking  
344 into account energy loss and multiple scattering.

- 345     • **Tagging ID tracks reconstruction:** Uses MS or calorimeter information to tag ID tracks  
 346                  as muons.
- 347     • **Combined track reconstruction:** Standalone muon tracks are extrapolated back to  
 348                  the vertex and matched to ID tracks within ( $|\eta| < 2.5$ ) and combined. This results in an  
 349                  improved momentum sensitivity from ID and MS information.

350       These strategies can be implemented in a variety of ways. There are two prominent fam-  
 351       ilies, STACO and MUID, that contain reconstruction packages which exploit one or a combi-  
 352       nation of these strategies. The STACO combined algorithm is used by the SMT tagger and is  
 353       described in more detailed below.

354       **STACO Combined Algorithm**

The STACO package combines ID and MS tracks by performing a statistical combination of the two independent tracks using track parameters ( $\eta, \phi, p_T, d_0, z_0$ ) and their covariance matrices. The quality of the fit is represented in the resulting  $\chi^2_{\text{match}}$ :

$$\chi^2_{\text{match}} = (\mathbf{T}_{\text{MS}} - \mathbf{T}_{\text{ID}})^T (\mathbf{C}_{\text{MS}} + \mathbf{C}_{\text{ID}})^{-1} (\mathbf{T}_{\text{MS}} - \mathbf{T}_{\text{ID}})$$

where  $\mathbf{T}_{\text{MS}}$  and  $\mathbf{T}_{\text{ID}}$  contain the track parameters for the MS track and the ID track respectively,

$$\mathbf{T}_{\text{MS or ID}} = \begin{pmatrix} \eta \\ \phi \\ p_T \\ d_0 \\ z_0 \end{pmatrix}$$

355       and  $\mathbf{C}_{\text{MS}}$  and  $\mathbf{C}_{\text{ID}}$  are the covariance matrices, defined as

$$\mathbf{C}_{ij} = (\mathbf{T}_i - \langle \mathbf{T}_i \rangle)(\mathbf{T}_j - \langle \mathbf{T}_j \rangle) \quad (1.4)$$

356       where  $\langle \mathbf{T}_i \rangle$  is the expectation value of  $\mathbf{T}_i$ . The full covariance matrix is included in Ap-  
 357       pendix ??.

Mode	Muon BR
$b \rightarrow \mu$	$10.95^{+0.29}_{-0.25} \%$
$b \rightarrow c \rightarrow \mu^+$	$8.02 \pm 0.19 \%$
$b \rightarrow \bar{c} \rightarrow \mu^-$	$1.6 \pm 0.5 \%$
$b \rightarrow \tau \rightarrow \mu$	$0.42 \pm 0.04 \%$
All modes	$21.0 \pm 1.0 \%$

Table 1.4: Branching ratio for the production of a muon from a  $b$ -quark in both direct and indirect modes [10].

358        If more than one possible combination per track exists, the best combined  $\chi^2_{\text{match}}$  is chosen  
 359        and then the track is removed from the pool of tracks to be match. The algorithm continues  
 360        making associations until no more tracks remain.

361        **Soft Lepton Tagging**

362        *Soft lepton tagging* (SLT) algorithms attempt to identify leptons produced in the semileptonic  
 363        decay of  $b$  and  $c$  quarks for the purpose of determining the presence of HF quarks. The term  
 364        “semileptonic” here refers to the decay of a  $b$ -hadron in such a way as to produce a lepton-  
 365        neutrino pair along with an additional hadron. The lepton produced would have a low- $p_T$  and  
 366        as such as is known as a soft lepton. SMT tagger exploits muons and as such these will be the  
 367        focus of the following discussion.

368        A soft muon can be produced in a variety of ways starting with a  $b$ -quark, either directly  
 369        via  $b \rightarrow \mu \bar{\nu}_\mu X$ , where  $X$  is any hadron; or indirectly, via a  $c$ ,  $\bar{c}$  or a  $\tau$  lepton. A summary  
 370        of the BR for each of these decays is shown in Table 1.4. The total BR for the production of  
 371        a soft muon from a  $b$  is  $20.1 \pm 0.1 \%$ , thus the probability for a  $t\bar{t}$  event to contain atleast one  
 372        semileptonically decaying  $b$  is approximately 38 %. The SMT tagger is described in detail in  
 373        Section ??.

---

# Bibliography

- 374 [1] Lyndon Evans and Philip Bryant. Lhc. *Journal of Instrumentation*, (08):S08001.
- 376 [2] The ATLAS Collaboration. Luminosity determination in pp collisions at  $\sqrt{s}=7$  tev  
377 using the atlas detector at the lhc. *The European Physical Journal C*, 71(4), 2011.
- 378 [3] ATLAS Collaboration. The ATLAS experiment at the CERN Large Hadron Collider. *Jour-*  
379 *nal of Instrumentation*, 3(08):S08003, 2008.
- 380 [4] ATLAS detector and physics performance: Technical Design Report, 1, 1999.
- 381 [5] M. A. Dobbs, S. Frixione, E. Laenen, K. Tollefson, H. Baer, E. Boos, B. Cox, R. Engel,  
382 W. Giele, J. Huston, S. Ilyin, B. Kersevan, F. Krauss, Y. Kurihara, L. Lonnblad, F. Mal-  
383 toni, M. Mangano, S. Odaka, P. Richardson, A. Ryd, T. Sjostrand, P. Skands, Z. Was, B. R.  
384 Webber, and D. Zeppenfeld. Les houches guidebook to monte carlo generators for hadron  
385 collider physics. *arXiv:hep-ph/0403045*, 2004.
- 386 [6] A. Schaelicke, T. Gleisberg, S. Hoeche, S. Schumann, J. Winter, F. Krauss, and G. Soff.  
387 Event generator for particle production in high-energy collisions. *Progress in Particle and*  
388 *Nuclear Physics*, 53(1):329–338, 2004.
- 389 [7] D.H. Perkins. *Introduction to High Energy Physics*. Cambridge University Pres, 2000.
- 390 [8] D. Griffiths. *Introcution to Elementary Particles*. John Wiley & Sons, Inc, 1987.
- 391 [9] B Resende. Muon identification algorithms in ATLAS, Sep 2009.
- 392 [10] Particle Data Group, J. Beringer, et al. The Review of Particle Physics. *Physical Review D*,  
393 86:010001+, 2012.